Geophysical Research Letters

RESEARCH LETTER
10.1029/2019GL085990

Biophysical Consequences of a Relaxing Beaufort Gyre

Jinlun Zhang[1], Yvette H. Spitz[2], Michael Steele[1], Carin Ashjian[3], Robert Campbell[4], and Axel Schweiger[1]

[1]University of Washington, Seattle, WA, USA, [2]Oregon State University, Corvallis, OR, USA, [3]Woods Hole Oceanographic Institution, Woods Hole, MA, USA, [4]University of Rhode Island, Kingston, RI, USA

Abstract A biophysical model shows that Beaufort Gyre (BG) intensification in 2004–2016 is followed by relaxation in 2017–2018, based on a BG variability index. BG intensification leads to enhanced downwelling in the central Canada Basin (CCB) and upwelling along the coast. In the CCB, enhanced downwelling reduces nutrients, thus lowering primary productivity (PP) and plankton biomass. Enhanced upwelling along the coast and in parts of the Chukchi shelf/slope increases nutrients, leading to elevated PP/biomass in the Pacific Arctic Ocean (PAO) outside of the CCB. The overall PAO PP/biomass is dominated by the shelf/slope response and thus increases during BG intensification. As the BG relaxes in 2017–2018, these processes largely reverse, with increasing PP/biomass in the CCB and decreasing PP/biomass in most of the shelf/slope regions. Because the shelf/slope regions are much more productive than the CCB, BG relaxation has the tendency to reduce the overall production in the PAO.

Key Points:
- An index indicates Beaufort Gyre relaxation in 2017–2018, with reduced Canada Basin downwelling and coastal upwelling
- Beaufort Gyre intensification (relaxation) leads to lower (higher) plankton biomass in Canada Basin and higher (lower) biomass in shelves
- Overall primary productivity in the Pacific Arctic increases (decreases) with Beaufort Gyre intensification (relaxation)

Supporting Information:
- Supporting Information S1

Correspondence to:
J. Zhang,
zhang@apl.washington.edu

Citation:
Zhang, J., Spitz, Y. H., Steele, M., Ashjian, C., Campbell, R., & Schweiger, A. (2020). Biophysical consequences of a relaxing Beaufort gyre. *Geophysical Research Letters*, *47*, e2019GL085990. https://doi.org/10.1029/2019GL085990

Received 24 OCT 2019
Accepted 16 DEC 2019
Accepted article online 19 DEC 2019

1. Introduction

Large-scale circulation in the Pacific Arctic Ocean (PAO; see Figure 1a for definition) is closely associated with the anticyclonic Beaufort Gyre (BG) located over the Canada Basin. Observations and model results indicate that the BG intensified in recent years; this intensification is associated with increased ocean velocity and freshwater content (FWC) in much of the PAO because of enhanced Ekman transport convergence and downwelling in the Canada Basin (CB) and enhanced upwelling in the Chukchi and Beaufort shelf and slope region (e.g., Giles et al., 2012; Krishfield et al., 2014; McPhee, 2013; Proshutinsky et al., 2009; Regan et al., 2019; Yang, 2009). However, there have been signs that the BG circulation began to stabilize in 2008 or 2009 (Armitage et al., 2017; Zhang et al., 2016).

The enhanced downwelling in the CB and upwelling in the Chukchi and Beaufort shelf and slope region likely have an impact on the planktonic ecosystem in the PAO. For example, based on observations taken in 2008, Coupel et al. (2015) reported that the CB during BG intensification showed a reduction in primary productivity (PP) because of a deepened nitracline (also see McLaughlin & Carmack, 2010), whereas areas with reduced freshening exhibited relatively high PP and phytoplankton biomass because of a shallower nitracline. While the impact of sea ice decline on Arctic PP and the planktonic ecosystem has been well recognized (e.g., Arrigo et al., 2008; Zhang et al., 2010; Jin et al., 2016), the impact of BG intensification and associated changes in the upwelling/downwelling pattern on PP and the planktonic ecosystem in the PAO has not been analyzed in a systematic manner on a decadal time scale. Even less known is the impact on the PAO planktonic ecosystem if significant BG relaxation occurs. Here a pan-Arctic biophysical model, the *B*iology-*I*ce-*O*cean *M*odeling and *A*ssimilation *S*ystem (BIOMAS, Zhang et al., 2015), is used to examine changes in BG circulation and upper ocean physics during the period 1992–2018 and to assess how these changes affect the spatiotemporal variability of the planktonic ecosystem.

2. Brief Model Description

BIOMAS has been included in a number of community ecosystem model intercomparison studies (e.g., Jin et al., 2016; Lee et al., 2016). It consists of a sea ice model, an ocean circulation model, a pelagic biological model, and a sea ice algae model. The pelagic biological model has 11 components: two phytoplankton classes (diatoms and flagellates), three zooplankton classes (microzooplankton, copepods, and predatory zooplankton), dissolved and detrital particulate organic nitrogen, detrital particulate organic silica, nitrate, ammonium, and silicate (Zhang et al., 2015). The sea ice algae model, based on Jin et al. (2006), has two ice

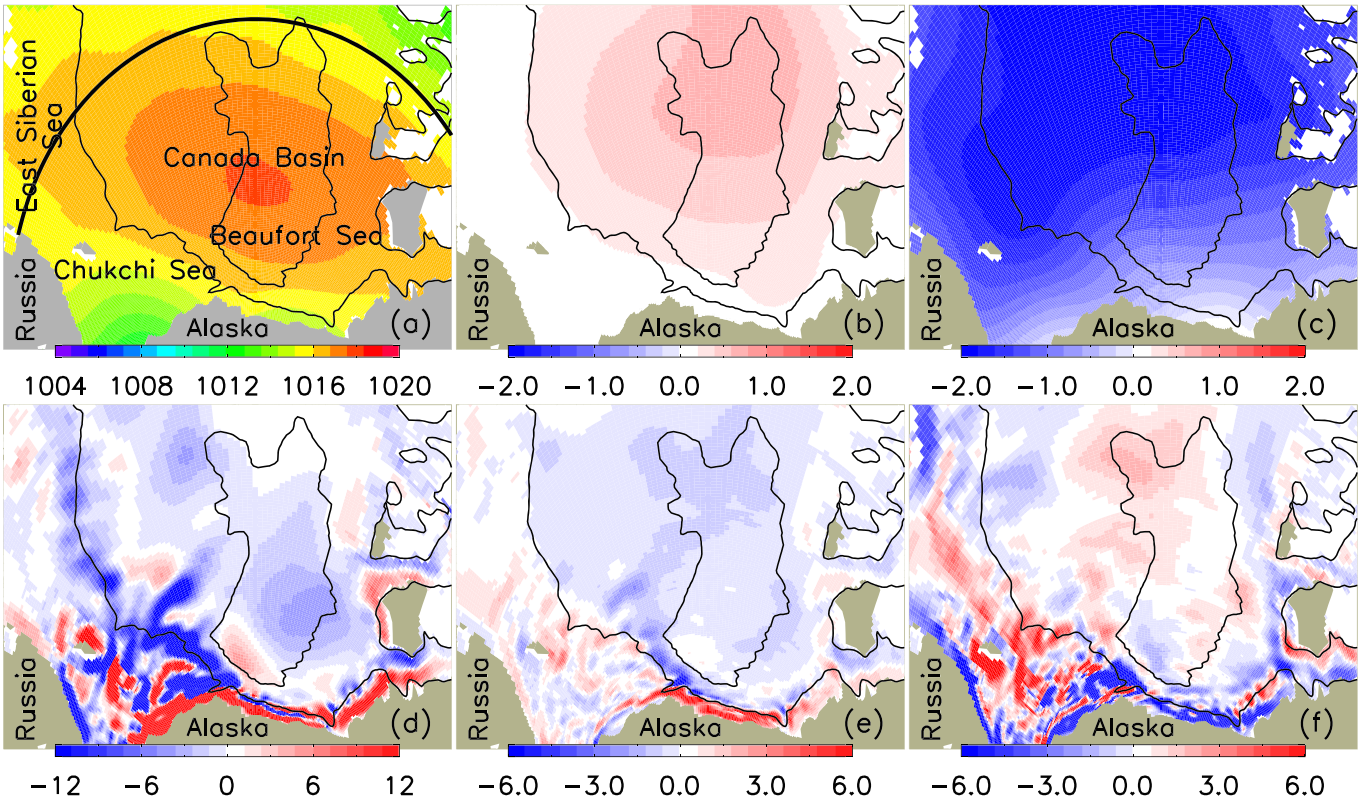

Figure 1. 1992–2018 mean CFS reanalysis SLP (mbar) (a) and the differences in SLP between the 2004–2016 mean and the 1992–2018 mean (b) and between the 2017–2018 mean and the 1992–2018 mean (c). simulated 1992–2018 mean Ekman upwelling velocity ($w_E = \nabla\times\tau/\rho f$, cm day^{-1}) (d) and the differences in Ekman upwelling velocity between the 2004–2016 mean and the 1992–2018 mean (e) and between the 2017–2018 mean and the 1992–2018 mean (f). the thin black lines represent isobaths of 100 and 3,600 m, respectively, based on the international bathymetric chart of the Arctic Ocean (IBCAO, Jakobsson et al., 2008). For the purpose of analysis, the Pacific Arctic Ocean is defined as the area enclosed by Bering Strait and a thick black line in (a). major topographic regions also are shown.

algal components (diatoms and flagellates), with nitrate, ammonium, and silicate as limiting nutrients for ice algal growth in a 2-cm layer at the sea ice bottom. The ocean model is based on the Parallel Ocean Program (Smith et al., 1992). The sea ice model is adapted from the Pan-arctic Ice-Ocean Modeling and Assimilation System (Zhang & Rothrock, 2003), with melt ponds incorporated (Zhang et al., 2018). BIOMAS assimilates satellite observations of sea ice concentration and sea surface temperature. It is forced by the National Oceanic and Atmospheric Administration 's Climate Forecast System (CFS) reanalysis data (Saha et al., 2010) over the period 1979–2018. More BIOMAS details are given in Zhang et al. (2015), Jin et al. (2016), and Lee et al. (2016), including model components, configuration, and initial conditions. Results over 1992–2018 are analyzed.

3. Model Evaluation and Results

In addition to assimilating satellite observations of sea ice concentration and sea surface temperature, BIOMAS sea ice velocity is calibrated with buoy drift data (http://iabp.apl.washington.edu) over the period 1992–2010, with a mean model ice speed bias of −6% and model-buoy speed correlation of 0.82. BIOMAS-simulated isohaline (salinity = 31 psu) depth has a mean bias of ~7 m (supporting information Figure S1) when compared to corresponding CTD (conductivity, temperature, and depth) observations in the central CB over the period 2003–2013 (Timmermans et al., 2014). The bias may be an indication that the model overestimates vertical mixing, in turn leading to a bias in PP. However, BIOMAS is able to capture most of the interannual variability of the CTD-derived isohaline depth, a measure of BG variability (Timmermans et al., 2014). When compared to available National Aeronautics and Space Administration IceBridge observations of sea ice thickness over the period 2012–2018 (supporting information Figure S2), BIOMAS shows a mean bias of 0.13 m (5%), with a model-observation correlation $R = 0.64$.

A comparison of BIOMAS-simulated chlorophyll *a* (mg m^{-}2) integrated over the upper 100 m with corresponding observations compiled by the PacMARS project (Grebmeier et al., 2015) over 1993–2012 indicates that most model results are relatively close to observations, especially in the region under study (supporting information Figure S3). However, the model also substantially overestimates or underestimates chlorophyll biomass in the upper 100 m at many observation locations, resulting in a large scatter in the plot of Figure S3. In particular, the model's inability to reproduce many of the observed large biomass values indicates the difficulty in comparing grid-cell-scale model results with point measurements. This was also reflected in the model-data intercomparison study of Lee et al. (2016) that used 21 biophysical models and a range of Arctic observations. This difficulty is often an important source of model bias, in addition to model uncertainties in forcing and parameterization. Overall, the model has a mean bias of -21.8 mg m^{-2} or 23% and the model-observation correlation is 0.35. A comparison of BIOMAS-simulated maximum chlorophyll *a* (mg m^{-3}) in the water column with corresponding observations compiled by the PacMARS project over 1993–2012 (supporting information Figure S4) has similar features to those shown in Figure S3. The model has a mean bias of -1.3 mg m^{-3} or 30%, and the model-observation correlation is 0.42.

BIOMAS simulates a general increase in the speed of ocean currents in the upper 100 m of the PAO (defined in Figure 1a) over 1992–2018 (Figure 2a). This is consistent with previous reports of stronger geostrophic currents in the CB in recent years (e.g., McPhee, 2013; Zhong et al., 2018). In particular, the simulated current speed increases in 2007, remains high until 2011, decreases in 2012–2013, and then climbs again in 2014, agreeing qualitatively with the 2003–2014 observations of Armitage et al. (2017). The general increase in current speed is largely due to BG intensification, that is, the Ekman convergence of freshwater into the center of the BG which enhances the large-scale lateral density gradients and thus geostrophic currents (e.g., McPhee, 2013; Zhong et al., 2018).

This BG intensification is driven by changes in the atmospheric forcing, characterized in the PAO by a Beaufort high-pressure cell (Figure 1a) with an anticyclonic surface wind circulation. After a sharp increase in the Climate Forecast System reanalysis sea level pressure (SLP) over the PAO in 2004, there are more strongly positive annual mean SLP anomalies (defined here as higher than 1 mbar) during 2004–2016 (six in total) than 1992–2003 (one only) (Figure 2b). This indicates an intensified Beaufort high in the later period (Figure 1b) (e.g., Wood et al., 2015), with strengthened anticyclonic BG circulation reflected in relatively high magnitudes of current speed and relative vorticity (defined as $-\nabla \times \boldsymbol{u}$, where $\boldsymbol{u}$ is horizontal ocean velocity averaged over the upper 100 m) (Figure 2a). Note that although the average SLP in the PAO is often higher in 2004–2016 than in 1992–2003, it drops considerably in 2015 (Figure 2b). However, the magnitudes of current speed and vorticity only decrease moderately in 2015, likely due to the long time scale of geostrophic current change in responding to changes in lateral density gradients (Johnson et al., 2018). In 2016, the average SLP remains low, so that the magnitude of vorticity continues to decrease in contrast to the current speed, which rebounds to some degree.

The average SLP in the PAO continues to drop to near the lowest level of the whole study period in 2017, although it rebounds a little in 2018 (Figure 2b; also see Figure 1c). The sustained decrease in SLP from 2015 to 2018 (Figure 2b) leads to a noticeable reduction in the magnitude of both ocean current speed and vorticity in 2017–2018 (Figure 2a). This period can be contrasted with the briefer reduction in SLP seen in 2012–2013, when current speed is reduced (also see Armitage et al., 2017) but ocean vorticity is relatively unchanged.

To help describe changes in BG circulation, a BG variability (BGV) index (Figure 2c) is constructed based on the depth of an isohaline ($S = 31$ psu) averaged over the area within 135–160°W and 74–83°N in the central CB. The BGV index is defined as the anomaly of annual mean depth of the isohaline in the area normalized by dividing the largest absolute value of the anomaly. The calculation of the BGV index is straightforward because of the fixed area, and moderately adjusting the area would not radically change the outcome. The BGV index (Figure 2c) shows mostly negative values in 1992–2003 and mostly positive values in 2004–2016, a sign of BG intensification. In 2017–2018, the index becomes negative again, a sign of BG relaxation (Figure 2c). Thus, the two periods (2004–2016 and 2017–2018) are useful to highlight spatiotemporal changes related to BG intensification and relaxation. The BGV index is well correlated with PAO ocean speed ($R = 0.95$) and vorticity ($R = 0.86$) averaged over the upper 100 m (Figure 2a).

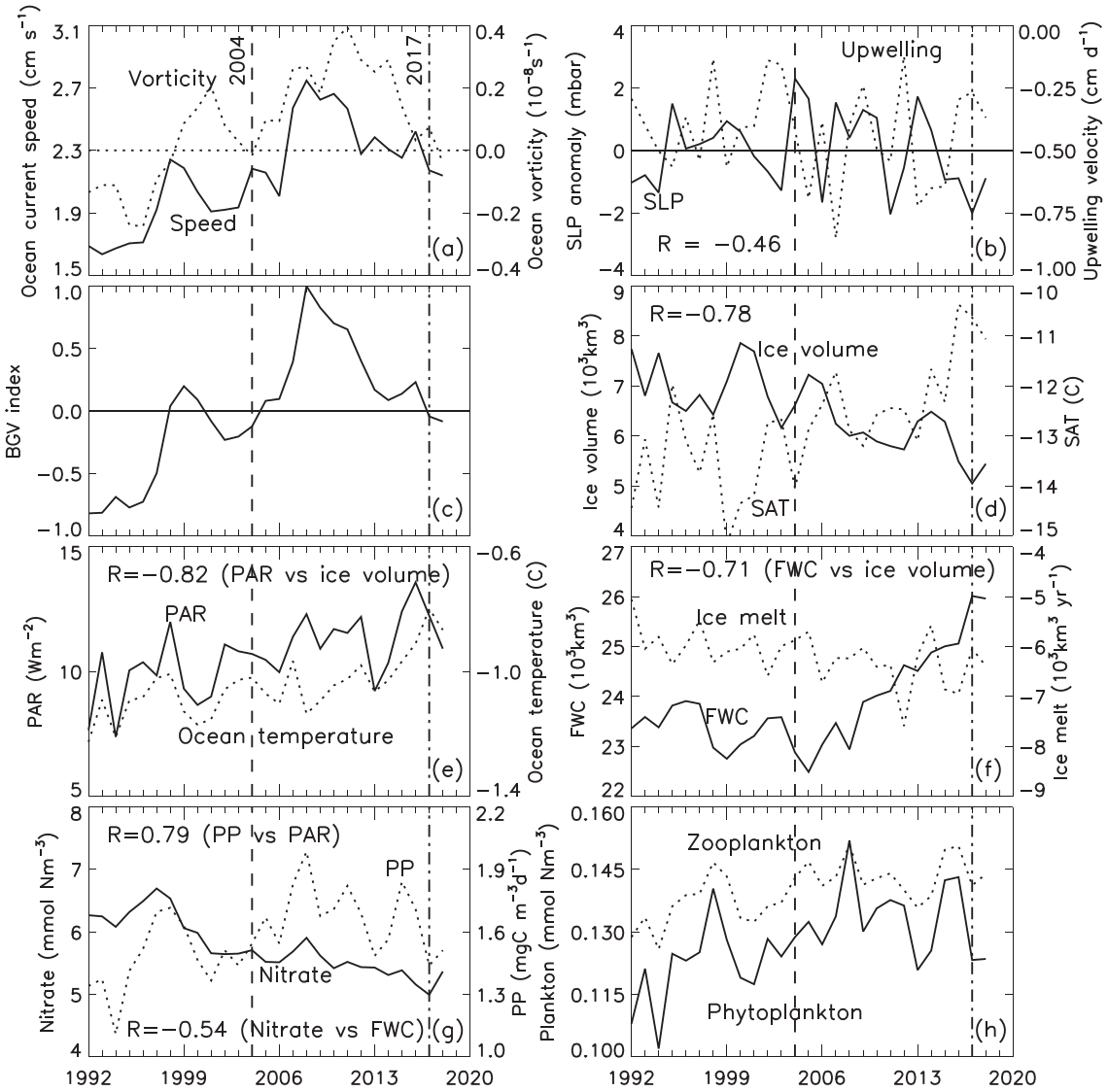

Figure 2. Annual mean time series for (a) simulated ocean current speed and relative vorticity over the upper 100 m (or from the surface to the bottom if shallower than 100 m), (b) CFS reanalysis sea level pressure (SLP) anomaly and simulated Ekman upwelling velocity (w_E), (c) Beaufort gyre variability (BGV) index defined as the anomaly of annual mean depth of the isohaline ($S = 31$ psu) normalized by dividing the largest absolute value of the anomaly, (d) simulated sea ice volume and CFS reanalysis surface air temperature (SAT), and simulated (e) photosynthetically active radiation (PAR) at the ocean surface and ocean temperature in the upper 100 m, (f) freshwater content (FWC) above the isohaline of $S = 34.8$ psu in the upper 100 m and annual ice melt from may to September, (g) nitrate concentration and primary productivity (PP) in the upper 100 m, and (h) phytoplankton and zooplankton in the upper 100 m, all averaged over the entire Pacific Arctic Ocean defined in Figure 2a except the BGV index that is averaged over the area within 135–160°W and 74–83°N. some correlation values are listed in (b) and (d)–(g) with p values at or below 0.02. Horizontal lines represent zero values for ocean vorticity (a), SLP anomaly (b), and BGV index (c). vertical dashed and dash-dotted lines represent years 2004 and 2017.

Changes in SLP and the anticyclonic wind circulation affect upwelling and downwelling caused by the divergence (upwelling) or convergence (downwelling) of Ekman transport within the surface layer (Yang, 2009). The simulated Ekman upwelling velocity is calculated as $w_E = \nabla\times\tau/\rho f$, where τ is ocean surface stress calculated following Martin et al. (2014), ρ is water density, and f is the Coriolis parameter. This method was shown by Zhong et al. (2018) to be highly correlated with similar methods that explicitly take into account the recent acceleration of geostrophic currents in the BG. The upwelling velocity is negative on average in the PAO (Figure 2b), indicating that downwelling dominates. Although the simulated w_E is characterized by negative values (downwelling) over a large area of the CB, positive values (upwelling) occur over a

much narrower region along the coast, with patches of negative and positive values in the Chukchi shelf and slope region (Figure 1d). Overall, the PAO-averaged w_E is negative and is negatively correlated with the PAO-averaged SLP ($R = -0.46$, p value = 0.02; Figure 2b), for example, a stronger atmospheric Beaufort High leads to stronger downwelling in the central CB.

As the BG intensifies over 2004–2016 with more positive SLP anomalies than in 1992–2003, there are more years of relatively strong downwelling on average over the PAO, such as 2005, 2007, and 2013–2015 (Figure 2b). Ekman downwelling is enhanced in the CB and upwelling is enhanced along the coast during 2004–2016 (Figure 1e), when compared to the 1992–2018 mean. In part of the Chukchi shelf and slope region, upwelling is increased. However, in 2017–2018, downwelling is reduced in most of the CB and upwelling is reduced along the coast (Figure 1f). In part of the Chukchi shelf and slope region, upwelling remains increased. Because the CB has a larger area than the coast, the magnitude of the PAO-averaged w_E is reduced considerably (Figure 2b).

The model also shows decreasing sea ice extent, sea ice volume, and snow volume in the PAO during 1992–2018, in conjunction with increasing surface air temperature forcing (Figure 2d). Compared to 1992–2018, ice is thinner in most of the PAO except the central CB in 2004–2016 (Figures 3a–3b) and continues to thin in 2017–2018, most strongly in the central CB (Figure 3c). The decrease in sea ice and snow leads to an increase in light penetration through ice (Figure 2e). The increasing photosynthetically active radiation (PAR) at the ocean surface, averaged over the PAO, is correlated negatively ($R = -0.82$) with decreasing ice volume (Figure 2e). Spatially, the increase in PAR is closely correlated with the decrease in ice thickness (not shown).

The declining sea ice cover contributes to a general increase in upper ocean temperature in the PAO over 1992–2018 (Figure 2e). In 2004–2016, the water temperature increases mostly in the shelf regions. There is a slight decrease of the mean ocean temperature over the upper 100 m in the central CB, forced by enhanced convergence and downwelling of cold surface waters there (Figures 3d and 3e). In 2017–2018, water temperature rebounds in the central CB because of BG relaxation (Figure 3f). Water temperature continues to increase over the shelves, owing to a decrease in sea ice and enhanced downward atmospheric heat fluxes (Figures 2d and 3e), which is favorable for phytoplankton growth.

Increasing summer ice melt and changes in Ekman dynamics jointly lead to increasing FWC in the PAO since 2005 (Figure 2f). The simulated FWC is relatively high in the central CB and low elsewhere (Figure 3g) because of surface convergence. As the BG intensifies in 2004–2016, FWC becomes much higher in the central CB and somewhat lower in surrounding areas because of enhanced water convergence toward the central CB (Figure 3h). As the BG relaxes in 2017–2018, the opposite occurs, with the central CB losing freshwater and the surrounding areas gaining freshwater (Figure 3i). Thus, Ekman dynamics provides only a simple spatial redistribution of FWC over the total PAO region. On the other hand, FWC in the upper 100 m of the PAO keeps increasing (Figure 2f) over this time period, owing to a general increase in ice melt, with particularly strong increase in 2015–2016 (Figure 2f) right before BG relaxation in 2017–2018. The increasing FWC is correlated ($R = -0.71$) with decreasing ice volume (Figure 2f).

Increasing FWC is also correlated with generally decreasing nitrate concentration in the upper 100 m of the PAO over 1992–2018 ($R = -0.54$) (Figure 2g) because of a deepened nitracline (e.g., Coupel et al., 2015; McLaughlin & Carmack, 2010). The simulated nitrate concentration is lower in the central CB and the East Siberian Sea and higher in the Chukchi Sea (Figure 4a). As the BG intensifies during 2004–2016, nitrate concentration is reduced in the CB and increased in the Chukchi Sea and coastal areas in the Beaufort Sea (Figures 4a and 4b), owing to enhanced downwelling in the basin and upwelling along the coast and in part of the Chukchi shelf and slope region. Note that enhanced downwelling in the deep basin is associated with enhanced lateral fluxes (Ekman transport convergence) toward the basin from adjacent areas (shelf/slope regions). In the North Atlantic subtropical gyre, such enhanced lateral fluxes may lead to an increase in nutrients in the central area of the gyre (Doddridge & Marshall, 2018; Williams & Follows, 1998). In the BG, however, this increase does not happen because lateral nutrient fluxes are small due to the low level of simulated nitrate concentration in much the East Siberian Sea (Figure 4a) and high consumption of nutrients in the shelf/slope regions of the Chukchi and Beaufort seas as reflected in the elevated PP and plankton biomass (Figures 4e, 4h, and 4k).

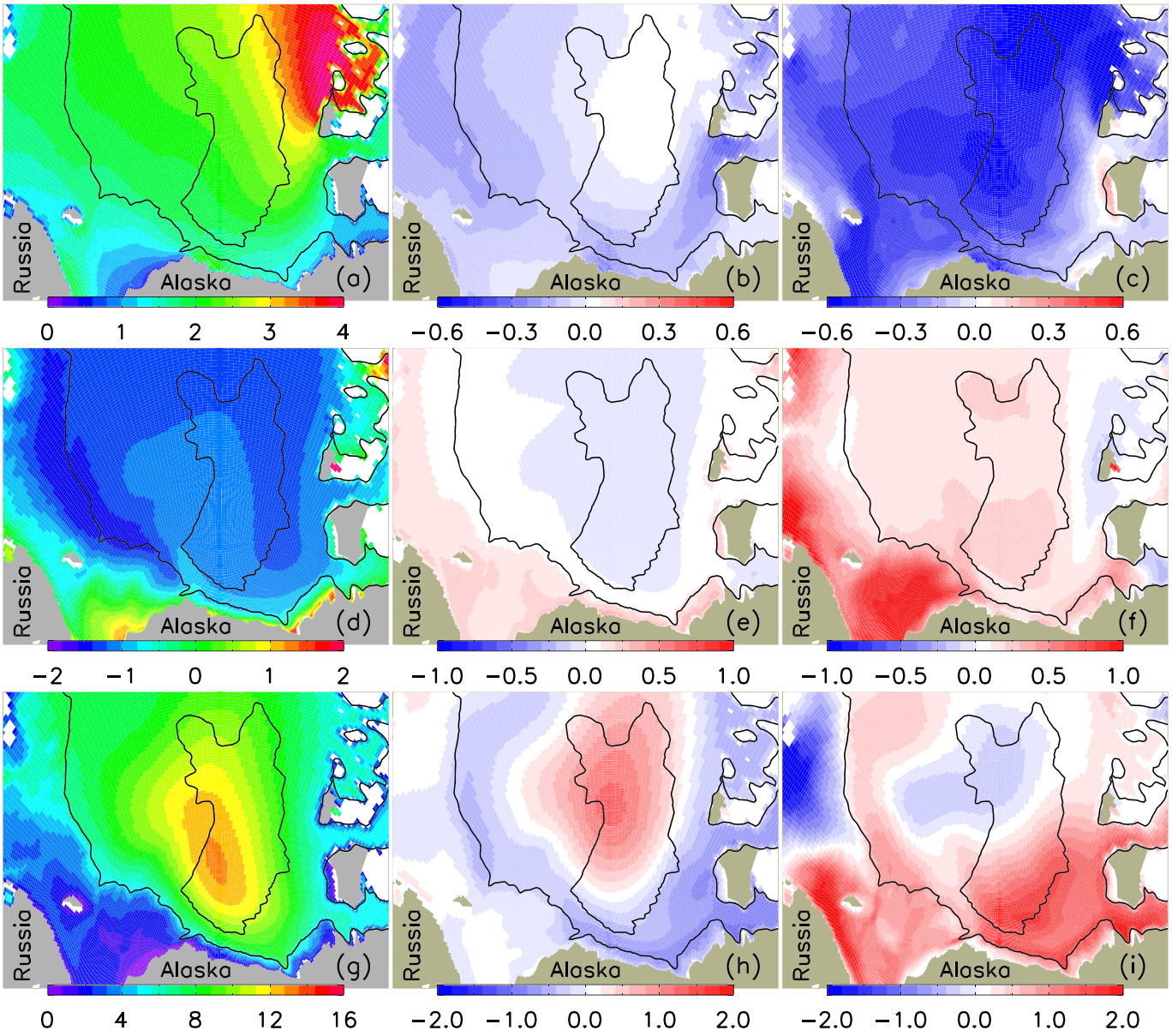

Figure 3. Simulated 1992–2018 mean sea ice thickness m (a) and the differences in sea ice thickness between the 2004–2016 mean and the 1992–2018 mean (b) and between the 2017–2018 mean and the 1992–2018 mean (c); same for the simulated mean and differences in ocean temperature (°C) in the upper 100 m (d–f) and freshwater content (m) above the isohaline of $S = 34.8$ psu in the upper 100 m (g–i).

When the BG relaxes in 2017–2018, the situation largely reverses, with the CB gaining nitrate and the Chukchi/Beaufort shelf region and the Beaufort slope region losing nitrate (Figure 4c). Meanwhile, nitrate in the Chukchi slope region is higher than the 1992–2018 mean, likely due to the fact that upwelling in 2017–2018 remains increased in part of the Chukchi shelf and slope region (Figure 1f). Because of BG relaxation, nitrate concentration averaged in the upper 100 m of the PAO rebounds in 2018 (Figure 2g), but not in 2017 when the model simulates a large drop in ice volume to its lowest level (Figure 2d), with a concurrent sharp increase in FWC (Figure 2f). This may have delayed the response of nitrate concentration in the upper ocean to the BG relaxation.

Although nutrient availability in the upper 100 m of the PAO is decreasing over 1992–2018, the simulated PP before 2017 is generally increasing (Figure 2g). The PP is correlated with PAR ($R = 0.79$; Figure 2e), the BGV index (0.75; Figure 2c), ocean speed (0.79; Figure 2a), vorticity (0.54; Figure 2a), and sea ice volume (−0.49, p

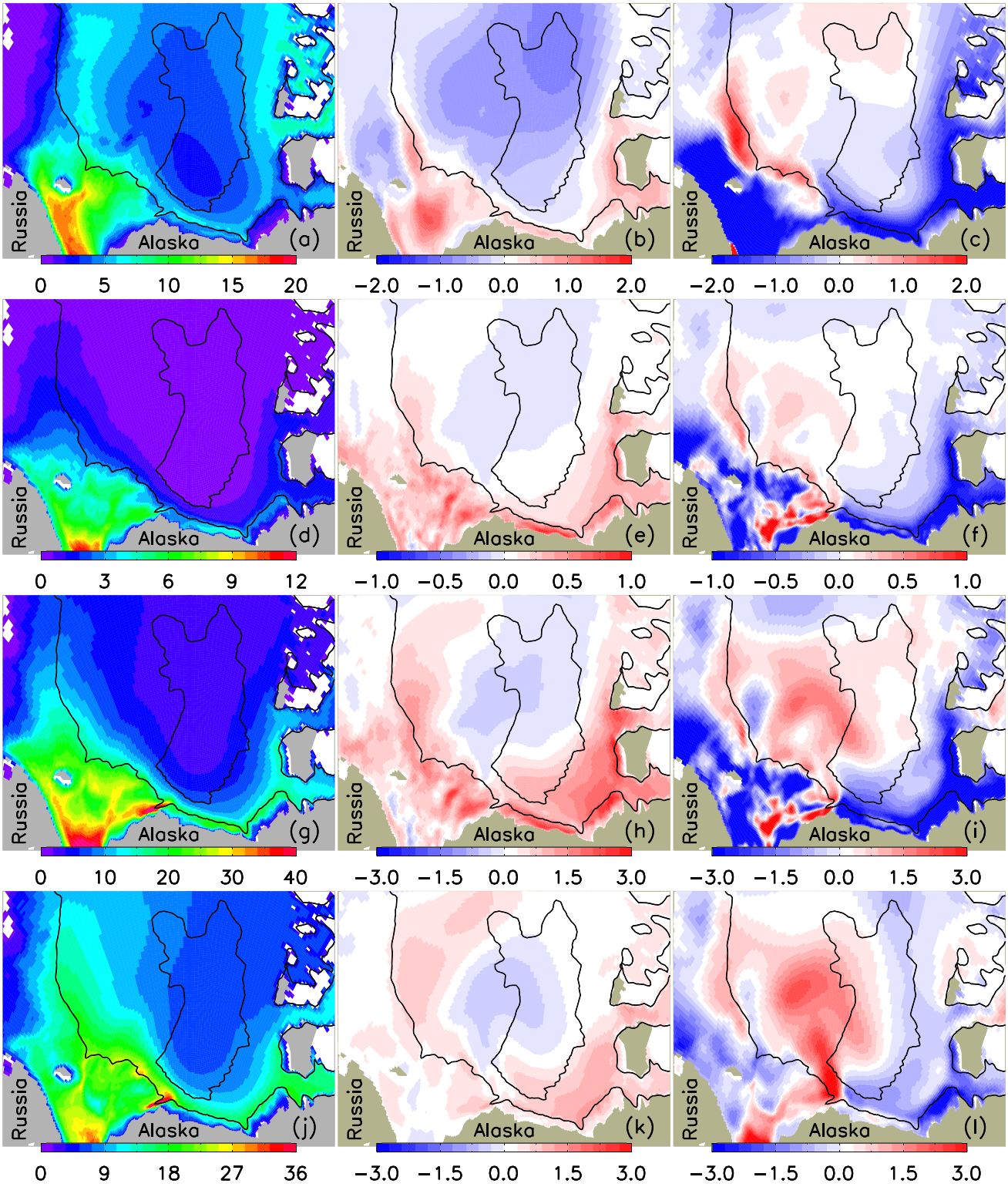

Figure 4. Simulated 1992–2018 mean nitrate concentration (mmol-N m^{-3}) (a) and the differences in nitrate concentration between the 2004–2016 mean and the 1992–2018 mean (b) and between the 2017–2018 mean and the 1992–2018 mean (c), averaged in the upper 100 m; same for the simulated mean and differences in primary productivity (mmol-N m^{-2} day^{-1}) (d–f), phytoplankton (mmol-N m^{-2}) (g–i), and zooplankton (mmol-N m^{-2}) (j–l), integrated in the upper 100 m.

value = 0.01; Figure 2d). However, it is only weakly correlated with ocean temperature (0.34, p value = 0.08; Figure 2e). The insignificant correlation with ocean temperature indicates that the impact of changes in temperature on PP is limited in the PAO. The estimated temperature-dependent growth rate does not change significantly (<3%) in the temperature range of the region.

Increasing PP leads to generally increasing phytoplankton and zooplankton biomass before BG relaxation starts in 2017 (Figure 2h). Not surprisingly, the PP is well correlated with phytoplankton (R = 0.92) and zooplankton (0.86). During BG intensification in 2004–2016, PP and plankton biomass decrease in the central CB and increase elsewhere in the PAO, particularly in the shelf regions (Figures 4d, 4e, 4g, 4h, 4j, and 4k). This is likely because of the combined effect of the increase in light availability and changes in water temperature (Figure 3e) and nitrate distribution (Figure 4b). During BG relaxation in 2017–2018, the model shows a large drop in average PP in 2017 and little rebound in 2018 (Figure 2g). The decreases in PP occur mostly in the areas away from the central CB, particularly in the shelf regions (Figure 4f) mainly because of reduced nutrient availability (Figure 4c). In the central CB, PP tends to increase because of reduced downwelling. These changes in PP are translated to changes in plankton biomass, which show increases in the central CB and decreases elsewhere, including most of the shelf region (Figures 4i and 4l). These increases in plankton biomass in the central CB are even somewhat more pronounced than the increase in PP. The concurrent increase in both phytoplankton and zooplankton biomass suggests a lack of grazer control of phytoplankton biomass, which is supported by previous studies in this region (Campbell et al., 2009; Sherr et al., 2009).

4. Concluding Remarks

This model study examines the response of the planktonic ecosystem in the PAO to the BG intensification and relaxation, including regional (e.g., shelf vs. basin) responses. Consistent with various previous studies (e.g., Armitage et al., 2017; Giles et al., 2012; Krishfield et al., 2014; McPhee, 2013; Regan et al., 2019; Zhang et al., 2016; Zhong et al., 2018), the model shows strong BG intensification during roughly the period 2004–2016. The BG intensification results from more frequent occurrence of a strong Beaufort high-pressure atmospheric cell driving a strengthened anticyclonic wind and ocean circulation, as reflected in mostly positive values of the BGV index constructed based on the depth of a isohaline (S = 31 psu) in the central CB. Model results further suggest that a significant relaxation of the BG has begun over the recent years 2017–2018. The BG relaxation is marked by negative values of the BGV index, with low SLP, ocean current speed and vorticity in the PAO.

The changes in BG circulation occurred at a time of sea ice decline, with a general increase in light availability at the ocean surface and in upper ocean temperature in the PAO, favorable for biological growth. The BG intensification with strengthened anticyclonic ocean circulation in 2004–2016 leads to enhanced Ekman transport convergence and downwelling in the central CB and enhanced upwelling along Alaskan coast. In the central CB, the enhanced Ekman transport convergence of surface cold waters reduces water temperature and increases FWC, while the enhanced downwelling reduces nutrient availability because of a deepened nitracline (e.g., Coupel et al., 2015; McLaughlin & Carmack, 2010), resulting in reduced PP and plankton biomass. In most of the shelf and slope regions of the PAO, the enhanced Ekman transport convergence of surface waters toward the central CB and the general decreases in ice thickness cause an increase in water temperature. The enhanced upwelling along the coast and in some Chukchi shelf and slope regions causes an increase in nutrient availability, which, together with increasing light availability and water temperature, leads to elevated PP and plankton biomass in most of the PAO away from the central CB.

As the BG relaxes and the anticyclonic ocean circulation weakens in 2017–2018, the physical processes are largely reversed. The model simulates reduced Ekman transport convergence and downwelling in the central CB and reduced upwelling along the coast, when compared with 2004–2016. The reduced Ekman transport convergence causes a reduction in FWC in the central CB and an increase in most of other areas of the PAO. There is no significant drop in the total FWC in the upper 100 m of the PAO in 2017–2018 because of continued freshwater contribution from a thinning sea ice cover. In addition, the simulated water temperature continues to increase throughout the PAO, including the central CB. These physical changes in turn result in enhanced PP and plankton biomass in the central CB and reduced PP and biomass in most of other areas of the PAO including most of the shelf and slope regions, even though water temperature and PAR

keep increasing there. Because the shelf and slope regions are much more productive than the central CB, BG relaxation in these recent years has the tendency to reduce the overall production in the PAO, as reflected in a drop in PP and biomass in 2017–2018 (Figures 2g and 2h). If the BG continues to relax in the future, we speculate that it may cause PP and plankton biomass to continue downward in the PAO. This could affect the CO_2 sink to the PAO and exacerbate warming of the PAO.

While model studies can shed light on changes in sea ice and upper ocean physics and how the changes may impact PP and the planktonic ecosystem in the PAO, it is essential to monitor the biophysical changes and possible interactions through satellite and in situ observations. Knowledge about the integrated system of sea ice, the upper ocean, and the planktonic ecosystem is still limited. It is necessary to learn more about the intertwining physical and biogeochemical processes in the PAO, for example, the close correlation between the BGV index and PP. This may be achieved by measuring changes in some of the key biophysical properties and linkages, such as changes in PP and the functioning of the planktonic ecosystem relative to changes in upwelling or downwelling and light or nutrient availability. These observations will enhance our understanding of the behavior of the integrated sea ice-ocean-biology system in a changing PAO with decreasing sea ice, increasing water temperature and FWC, and varying ocean circulation including BG intensification and relaxation. They will also help improve model representation of biophysical processes.

Acknowledgments
This work is funded by the NASA Cryosphere Program (NNX15AG68G and NNX17AD27G), the NSF Office of Polar Programs (PLR-1416920, PLR-1603259, PLR-1603266, OPP-1751363, PLR-1602521, and PLR-1503298), the NOAA Climate Program Office (NA15OAR4310170 and NA15OAR4320063AM170), and ONR (N00014-17-1-2545). We thank Drs. Benjamin Rabe and Edward Doddridge for their constructive comments and Kay Runciman for graphics support. CFS reanalysis data used for model forcing are available online (https://www.ncdc.noaa.gov/data-access/model-data/model-datasets/climate-forecast-system-version2-cfsv2). Model results are in https://pscfiles.apl.uw.edu/zhang/BIOMAS168x180/ website.

References

Armitage, T. W. K., Bacon, S., Ridout, A. L., Petty, A. A., Wolbach, S., & Tsamados, M. (2017). Arctic Ocean geostrophic circulation 2003–2014. *The Cryosphere*, *11*(4), 1767–1780. https://doi.org/10.5194/tc-2017-22

Arrigo, K. R., van Dijken, G., & Pabi, S. (2008). Impact of a shrinking Arctic ice cover on marine primary production. *Geophysical Research Letters*, *35*, L19603. https://doi.org/10.1029/2008GL035028

Campbell, R. G., Sherr, E. B., Ashjian, C. J., Plourde, S., Sherr, B. F., Hill, V., & Stockwell, D. A. (2009). Mesozooplankton prey preference and grazing impact in the western Arctic Ocean. *Deep Sea Research Part II: Topical Studies in Oceanography*, *56*(17), 1274–1289.

Coupel, P., Ruiz-Pino, D., Sicre, M. A., Chen, J. F., Lee, S. H., Schiffrine, N., et al. (2015). The impact of freshening on phytoplankton production in the Pacific Arctic Ocean. *Progress in Oceanography*, *131*, 113–125.

Doddridge, E. W., & Marshall, D. P. (2018). Implications of eddy cancellation for nutrient distribution within subtropical gyres. *Journal of Geophysical Research: Oceans*, *123*, 6720–6735. https://doi.org/10.1029/2018JC013842

Giles, K. A., Laxon, S. W., Ridout, A. L., Wingham, D. J., & Bacon, S. (2012). Western Arctic Ocean freshwater storage increased by wind-driven spin-up of the Beaufort gyre. *Nature Geoscience*, *5*(3), 194–197. https://doi.org/10.1038/NGEO1379

Grebmeier, J. M., Cooper, L. W., Ashjian, C. A., Bluhm, B. A., Campbell, R. B., Dunton, K. E., et al. (2015). Pacific Marine Arctic Regional Synthesis (PacMARS) final report, North Pacific Research Board (259 pp.).

Jakobsson, M., Macnab, R., Mayer, L., Anderson, R., Edwards, M., Hatzky, J., et al. (2008). An improved bathymetric portrayal of the Arctic Ocean: Implications for ocean modeling and geological, geophysical and oceanographic analyses. *Geophysical Research Letters*, *35*, L07602. https://doi.org/10.1029/2008GL033520

Jin, M., Deal, C. J., Wang, J., Shin, K. H., Tanaka, N., Whitledge, T. E., et al. (2006). Controls of the landfast ice–ocean ecosystem offshore Barrow, Alaska. *Annals of Glaciology*, *44*, 63–72.

Jin, M., Popova, E. E., Zhang, J., Ji, R., Pendleton, D., Varpe, O., et al. (2016). Ecosystem model intercomparison of under-ice and total primary production in the Arctic Ocean. *Journal of Geophysical Research: Oceans*, *121*, 934–948. https://doi.org/10.1002/2015JC010770

Johnson, H. L., Cornish, S. B., Kostov, Y., Beer, E., & Lique, C. (2018). Arctic Ocean freshwater content and its decadal memory of sealevel pressure. *Geophysical Research Letters*, *45*, 4991–5001. https://doi.org/10.1029/2017GL076870

Krishfield, R. A., Proshutinsky, A., Tateyama, K., Williams, W. J., Carmack, E. C., McLaughlin, F. A., & Timmermans, M.-L. (2014). Deterioration of perennial sea ice in the Beaufort gyre from 2003 to 2012 and its impact on the oceanic freshwater cycle. *Journal of Geophysical Research: Oceans*, *119*, 1271–1305. https://doi.org/10.1002/2013JC008999

Lee, Y. J., Matrai, P. A., Friedrichs, M. A. M., Saba, V. S., Aumont, O., Babin, M., et al. (2016). Net primary productivity estimates and environmental variables in the Arctic Ocean: An assessment of coupled physical-biogeochemical models. *Journal of Geophysical Research: Oceans*, *121*, 8635–8669. https://doi.org/10.1002/2016JC011993

Martin, T., Steele, M., & Zhang, J. (2014). Seasonality and long-term trend of Arctic Ocean surface stress in a model. *Journal of Geophysical Research: Oceans*, *119*, 1723–1738. https://doi.org/10.1002/2013JC009425

McLaughlin, F. A., & Carmack, E. C. (2010). Deepening of the nutricline and chlorophyll maximum in the Canada Basin interior, 2003–2009. *Geophysical Research Letters*, *37*, L24602. https://doi.org/10.1029/2010GL045459

McPhee, M. G. (2013). Intensification of geostrophic currents in the Canada Basin, Arctic Ocean. *Journal of Climate*, *26*(10), 3130–3138.

Proshutinsky, A., Krishfield, R., Timmermans, M.-L., Toole, J., Carmack, E., McLaughlin, F., et al. (2009). Beaufort Gyre freshwater reservoir: State and variability from observations. *Journal of Geophysical Research*, *114*, C00A10. https://doi.org/10.1029/2008JC005104

Regan, H. C., Lique, C., & Armitage, T. W. K. (2019). The Beaufort Gyre extent, shape, and location between 2003 and 2014 from satellite observations. *Journal of Geophysical Research: Oceans*, *124*, 844–862. https://doi.org/10.1029/2018JC014379

Saha, S., Moorthi, S., Pan, H. L., Wu, X., Wang, J., Nadiga, S., et al. (2010). The NCEP climate forecast system reanalysis. *Bulletin of the American Meteorological Society*, *91*(8), 1015–1058. https://doi.org/10.1175/2010BAMS3001.1

Sherr, E. B., Sherr, B. F., & Hartz, A. J. (2009). Microzooplankton grazing impact in the Western Arctic Ocean. *Deep Sea Research Part II: Topical Studies in Oceanography*, *56*(17), 1264–1273.

Smith, R. D., Dukowicz, J. K., & Malone, R. C. (1992). Parallel ocean general circulation modeling. *Physica D*, *60*, 38–61.

Timmermans, M.-L., Proshutinsky, A., Golubeva, E., Jackson, J. M., Krishfield, R., McCall, M., & Platov, G. (2014). Mechanisms of Pacific Summer Water variability in the Arctic's Central Canada Basin. *Journal of Geophysical Research: Oceans*, *119*, 7523–7548. https://doi.org/10.1002/2014JC0102

Williams, R. G., & Follows, M. J. (1998). The Ekman transfer of nutrients and maintenance of new production over the North Atlantic. *Deep Sea Research Part I: Oceanographic Research Papers*, *45*(2–3), 461–489. https://doi.org/10.1016/S0967-0637(97)00094-0

Wood, K. R., Bond, N. A., Danielson, S. L., Overland, J. E., Salo, S. A., Stabeno, P., & Whitefield, J. (2015). A decade of environmental change in the Pacific-Arctic region. *Progress in Oceanography*, *136*, 12–31. https://doi.org/10.1016/j.pocean.2015.05.005

Yang, J. (2009). Seasonal and interannual variability of downwelling in the Beaufort Sea. *Journal of Geophysical Research*, *114*, C00A14. https://doi.org/10.1029/2008JC005084

Zhang, J., Ashjian, C., Campbell, R., Spitz, Y. H., Steele, M., & Hill, V. (2015). The influence of sea ice and snow cover and nutrient availability on the formation of massive under-ice phytoplankton blooms in the Chukchi Sea. *Deep-Sea Research Part II*, *118*, 122–135. https://doi.org/10.1016/j.dsr2.2015.02.008

Zhang, J., & Rothrock, D. A. (2003). Modeling global sea ice with a thickness and enthalpy distribution model in generalized curvilinear coordinates. *Monthly Weather Review*, *131*(5), 681–697.

Zhang, J., Schweiger, A., Webster, M., Light, B., Steele, M., Ashjian, C., et al. (2018). Melt pond conditions on declining Arctic sea ice over 1979–2016: Model development, validation, and results. *Journal of Geophysical Research: Oceans*, *123*, 7983–8003. https://doi.org/10.1029/2018JC014298

Zhang, J., Spitz, Y. H., Steele, M., Ashjian, C., Campbell, R., Berline, L., & Matrai, P. (2010). Modeling the impact of declining sea ice on the Arctic marine planktonic ecosystem. *Journal of Geophysical Research*, *115*, C10015. https://doi.org/10.1029/2009JC005387

Zhang, J., Steele, M., Runciman, K., Dewey, S., Morison, J., Lee, C., et al. (2016). The Beaufort Gyre intensification and stabilization: A model-observation synthesis. *Journal of Geophysical Research: Oceans*, *121*, 7933–7952. https://doi.org/10.1002/2016JC01219

Zhong, W., Steele, M., Zhang, J., & Zhao, J. (2018). Greater role of geostrophic currents on Ekman dynamics in the western Arctic Ocean as a mechanism for Beaufort Gyre stabilization. *Journal of Geophysical Research: Oceans*, *123*, 149–165. https://doi.org/10.1002/2017JC013282